AMERICAN SOCIETY FOR MICROBIOLOGY | mBio

Check for updates

| Biotechnology | Research Article

Impact of oxidative stress on *Magnetospirillum gryphiswaldense* MSR-1 physiology and magnetosome biomineralization at the single-cell level

Marta Masó-Martínez,[1,2] Julika Radecke,[3] Craig MacGregor-Chatwin,[3] Paul D. Topham,[2] Alfred Fernández-Castané[1,2]

AUTHOR AFFILIATIONS See affiliation list on p. 16.

ABSTRACT Magnetotactic bacteria, such as *Magnetospirillum gryphiswaldense* MSR-1, naturally produce magnetosomes—intracellular magnetic nanoparticles that enable navigation within geomagnetic fields. Magnetosomes hold significant potential for biomedical and biotechnological applications; however, key aspects of their biomineralization remain poorly understood. This study investigates how oxidative stress, induced by hydrogen peroxide and iron, influences magnetosome formation and bacterial physiology under aerobic and microaerobic conditions. Single-cell advanced microscopy and high-throughput techniques revealed that microaerobic conditions supported robust magnetosome production and larger magnetite crystals while maintaining low oxidative stress levels. In contrast, aerobic conditions suppressed magnetosome formation, reduced intracellular iron content, and increased reactive oxygen species (ROS) levels. High extracellular iron enhanced the formation of longer magnetosome chains in microaerobic cultures without causing toxicity but reduced cell viability under aerobic conditions. Hydrogen peroxide exposure caused mild damage and a 25% viability drop in magnetosome-producing cells but led to severe damage and an 80% viability drop in non-magnetosome-producing cells, along with chain fragmentation and smaller magnetite crystals. These results suggest that magnetosome-producing cells exhibit greater resilience to oxidative stress, potentially due to ROS scavenging properties of magnetosomes, and highlight the intricate interplay between oxidative stress, iron regulation, and magnetosome biomineralization. Single-cell analysis revealed heterogeneity in physiological responses, further demonstrating the complexity of these processes. These findings underscore the importance of monitoring physiological changes during production processes to enhance the efficiency and robustness of magnetosome synthesis. The insights gained provide a foundation for improving bioprocesses for large-scale production of high-quality magnetosomes, advancing their applications in biomedicine and biotechnology.

IMPORTANCE Magnetotactic bacteria (MTB) are fascinating microorganisms with the capacity to produce iron oxide nanomagnets, namely magnetosomes. These nanomagnets passively align with magnetic fields, providing the basis for magnetic guidance when coupled with bacterial motility. This unique feature has inspired the concept of MTB as a self-propelled medical device to deliver therapeutic cargo. To this end, survival in physiological conditions and other microenvironments is essential. This study reveals the interplay between MTB physiology and magnetosome biomineralization subject to oxidative stress and varying environmental conditions, employing a holistic multi-parametric approach. Our results provide an in-depth understanding of the metabolic and physiological mechanisms at the single-cell level. This is crucial to develop more robust MTB biomanufacturing strategies to produce bacteria that possess the required quality

Editor Danielle A. Garsin, The University of Texas Health Science Center at Houston, Houston, Texas, USA

Address correspondence to Marta Masó-Martínez , m.masomartinez@aston.ac.uk, or Alfred Fernández-Castané, a.fernandez-castane1@aston.ac.uk.

The authors declare no conflict of interest.

See the funding table on p. 16.

Received 3 November 2025
Accepted 5 December 2025
Published 29 December 2025

attributes, thus paving the way for future biotechnological and biomedical application studies.

KEYWORDS magnetotactic bacteria, magnetosomes, biomineralization, correlative microscopy, cryo-electron tomography, oxidative stress

Oxidative stress is a consequence of the excessive production of reactive oxygen species (ROS), which are the by-products of oxygen reduction in metabolic processes (1). Organisms residing in oxygen-rich environments have developed scavenging systems to mitigate this oxidative stress (2). However, when ROS accumulation surpasses the cellular antioxidant defense mechanisms, it can lead to damage to nucleic acids, proteins, lipids, and other cellular components, directly compromising cell viability (3). Controlling ROS accumulation is thus a critical parameter in bioprocessing. Excessive ROS not only affects cell health and viability but also induces oxidative modifications that can affect product quality, introduce variability in cell growth, and limit productivity. Therefore, the activation of cellular stress responses that alter metabolism and cell behavior can further impact the efficiency and consistency of the bioprocess.

The magnetic nanoparticles naturally produced by magnetotactic bacteria (MTB), called magnetosomes, represent an attractive alternative to chemically synthesized magnetic nanoparticles for biomedical, biotechnological, and environmental applications due to their unique properties (4). Magnetosomes are intracellular membrane-enveloped magnetic nanosized crystals of either magnetite (Fe_3O_4) or greigite (Fe_3S_4), depending on the species, typically arranged in a needle-like chain that acts as a compass needle, enabling an active orientation within the Earth's magnetic field. These properties make magnetosomes and their producing bacteria attractive for applications such as magnetic hyperthermia, theranostic devices, magnetic resonance imaging contrast agents, and bioremediation (5–8). Their uniform size, high crystallinity, and biocompatibility further enhance their potential for such applications, highlighting the relevance of studying their biosynthesis and cellular regulation.

Magnetosome synthesis involves a complex and highly regulated biomineralization process that requires large amounts of iron and optimal microaerobic conditions, typically around 25 mbar O_2 (approximately 0.1%–1% O_2) (9). However, elevated intracellular levels of iron ions can lead to significant oxidative stress as hydrogen peroxide (H_2O_2) reacts with ferrous iron (Fe^{2+}) in the so-called "Fenton reaction" to produce hydroxyl radicals (OH•) (10), which are among the most toxic ROS. Therefore, monitoring cell physiology during cell growth and magnetosome production is crucial to ensure cell viability and to control iron homeostasis to avoid the formation of specific physiological inhibitors, such as excessive ROS accumulation.

The mechanisms by which MTB tackle oxidative stress remain a significant and unresolved research question. Several studies have identified oxidative stress regulation mechanisms in these bacteria that are similar to those in other prokaryotic organisms. For instance, the presence of an OxyR-like redox-sensing transcription factor has been identified in some MTB species, such as *Magnetospirillum gryphiswaldense* MSR-1 and *Magnetospirillum magneticum* AMB-1 (11–13). Additionally, it has been observed that magnetosomes possess peroxidase-like activity, which could contribute to lowering overall ROS levels (14). This potential ROS-scavenging role of magnetosomes points to additional functions for magnetosome chains beyond their role in magnetic orientation.

In this study, we investigated the physiological responses of the MTB species *M. gryphiswaldense* MSR-1 to sudden oxidative perturbations to elucidate how cells cope with acute stress conditions. We hypothesized that magnetosome-producing bacteria would exhibit greater tolerance to oxidative challenges than non-producing bacteria, owing to the potential ROS-scavenging role of magnetosomes. To test this, MSR-1 cultures were exposed to H_2O_2 and high levels of extracellular iron (in the form of Fe(III)-citrate) while monitoring key physiological parameters, including cell viability, cell

growth, intracellular iron accumulation, polyhydroxyalkanoate (PHA) granule formation, and ROS accumulation.

A combination of complementary analytical techniques was applied to capture responses across scales. Flow cytometry (FCM) was employed as an in-line tool for the rapid assessment of the physiological state of MSR-1 cells, focusing on parameters such as cell viability, intracellular ROS and iron levels, and PHA formation; inductively coupled plasma optical emission spectroscopy (ICP-OES) was used as an offline tool to quantify magnetosome and iron content; correlative light and electron microscopy (CLEM) combined cryo-electron and cryo-fluorescence imaging to simultaneously visualize magnetosomes, ROS, and intracellular iron at the single-cell level. To the best of our knowledge, only a few correlative microscopy studies have been performed on MTB (15–17), but this represents the first to combine these methods in MTB, providing an integrated framework to investigate the relationship between ROS, the intracellular labile iron pool, and magnetosome content at the single-cell level. By integrating high-resolution and high-throughput techniques within a single experimental design, this study offers mechanistic insight into how MTB cope with acute oxidative stress and lays the groundwork for optimizing magnetosome and MTB biomanufacturing platforms.

MATERIALS AND METHODS

Strains, growth media, and culture conditions

M. gryphiswaldense MSR-1 (DMSZ 6631) was grown in flask standard medium (FSM), comprising 3.5 g·L^{-1} potassium L-Lactate, 0.1 g·L^{-1} KH_2PO_4, 0.15 g·L^{-1} $MgSO_4{\cdot}7H_2O$, 2.38 g·L^{-1} HEPES, 0.34 g·L–1 $NaNO_3$, 0.1 g·L^{-1} yeast extract, 3 g·L^{-1} soy bean peptone, 100 µM iron citrate ($C_6H_5FeO_7$), and 5 mL·L^{-1} EDTA-chelated trace elements solution (EDTA-TES). EDTA-TES solution consisted of 5.2 g·L^{-1} EDTA disodium salt; 30 mg·L^{-1} H_3BO_3; 85.4 mg·L^{-1} $MnSO_4{\cdot}H_2O$; 190 mg·L^{-1}; 2.1 g·L^{-1} $FeSO_4{\cdot}7H_2O$, $CoCl_2$ g·L^{-1}; 4 mg·L^{-1} $NiCl_2{\cdot}6H_2O$; 2 mg·L^{-1} $CuCl_2{\cdot}2H_2O$; 44 mg·L^{-1} $ZnSO_4{\cdot}7H_2O$; and 36 mg·L^{-1} $Na_2MoO_4{\cdot}2H_2O$. The pH of FSM and EDTA-TES was adjusted to 7.0 and 6.5, respectively, using 1 M NaOH prior to autoclaving.

MSR-1 cultures were grown in 100 mL DURAN bottles, each with a working volume of 90 mL, under aerobic and microaerobic conditions in an Incu-Shake MAXI (SciQuip Ltd, Newtown, UK) orbital shaker incubator set at 150 rpm and 30°C. Microaerobic conditions promote the formation of magnetosome-producing cells, whereas aerobic conditions inhibit magnetosome production, resulting in non-magnetosome-producing cells. To generate microaerobic conditions, bottles were purged with N_2 for 30 min to remove all the dissolved O_2 and sealed with bromobutyl rubber stoppers and later injected with the necessary sterile air volume to achieve~1% O_2. Aerobic bottles were left with their lids slightly loosened to allow free air exchange. Each bottle was inoculated at a 1:10 ratio and incubated for 60 h, with samples taken every 6–12 h for analysis. During the early exponential growth phase (OD_{565} = 0.15), a pulse of iron citrate (final iron concentration of 400 µM) or H_2O_2 (final concentration of 150 µM) was added to both aerobic and microaerobic cultures to induce oxidative stress. Experiments were carried out in triplicate. This sampling and stress-induction strategy was chosen to capture dynamic cellular responses during exponential growth while avoiding the lag or stationary phases, which might complicate interpretation. Applying stress at the early exponential phase ensures microaerobic cells already contain magnetosomes, whereas aerobic cells have ceased magnetosome production, allowing a meaningful comparison of oxidative stress effects in their presence or absence.

Bacterial growth and magnetic cellular response

Bacterial growth was assessed by measuring the optical density of cultures using an Evolution 300 UV-Vis spectrophotometer (Thermo Fisher Scientific, Hemel Hempstead, Herts, UK) at a wavelength of 565 nm (OD_{565}). The cellular magnetic response (C_{mag}) was evaluated according to a previously described method immediately after the OD_{565}

measurements (18). In brief, the spectrophotometer has two pairs of Helmholtz coils mounted on the cuvette holder, one pair oriented perpendicular to the light beam and the other parallel. For magnetic cells, the different alignments result in varying optical densities due to cell migration as a result of the applied magnetic field, whereas non-magnetic cells show no change when the magnetic field orientation is altered, thus maintaining constant optical density. C_{mag} values are then determined by the ratio of OD_{565} measurements for cells aligned parallel and perpendicular to the light beam. C_{mag} values range between 1 and 3, with values exceeding one, indicating the presence of magnetic cells.

Flow cytometry

Bacterial samples were collected from the liquid cultures, diluted in phosphate-buffered saline solution (PBS), and directly analyzed in a BD Accuri C6 flow cytometer (Becton, Dickinson and Company, Oxford, UK). Flow cytometry was employed to determine relative cell size (FSC-A), cell granularity/complexity (SSC-A), intracellular soluble iron concentration, cell viability, PHA formation, and ROS accumulation. The soluble intracellular iron pool was detected by incubating the cells with Phen Green SK fluorophore (PG-SK) (5 µM) for 10 min; PHA granules were stained with Pyrromethene-546 (Pyr-546) (0.5 µg/mL); cell viability was assessed by incubating the cells with propidium iodide (PI) (100 ng/mL) and bis (1.3-dibutybarbituric acid) trimethine oxonol (BOX) (100 ng/mL) for 2 min; and the presence of ROS was detected by incubating the cells for 30 min at 30°C with CellROX Deep Red (CRDR) fluorophore (5 µM). Cells stained with green (PG-SK, Pyr-546, BOX) and red fluorophores (PI) were excited with a 488 nm solid-state laser, with fluorescence detected using a 533/30 BP filter and a 670 LP filter, respectively. Far-red fluorescent labeled cells (CRDR) were excited with a 640 nm solid-state laser and detected through a 675/25 BP filter.

Determination of iron content

Inductively coupled plasma optical emission spectroscopy (Thermo Scientific iCAP 7000) coupled with a Teledyne CETAC ASX-520 Random Access Autosampler was employed as an offline analysis to monitor the changes in the intracellular and extracellular iron concentrations of MSR-1 cultures. One mL of each sample was centrifuged to separate cells from the culture media. Supernatants were acidified by adding 10 µL of nitric acid solution (70% vol/vol), whereas cell pellets were digested using 500 µL of the nitric acid solution and incubated at 98°C for 2 h with shaking at 300 rpm. After digestion, the final volume was re-adjusted to 1 mL by adding deionized water. Samples preparation was done and analyzed in triplicate.

Correlative light and electron microscopy

MSR-1 cells were grown until just before the end of their exponential growth phase. To detect intracellular iron and ROS accumulation, cells were incubated with PG-SK and CRDR, respectively. Vitrification of the samples was performed at the Electron Bio-Imaging Center (eBIC) located at Diamond Light Source, UK's synchrotron. Approximately 4 µL of the cell suspension was applied to the front of Quantifoil R2/2 grids, with 0.5 µL applied to the back. The grids were then blotted for 6 s using an EM GP2 Automatic Plunge Freezer (Leica Microsystems) before plunge freezing.

After sample vitrification, the grids were transferred to a Leica EM cryoCLEM microscope (Leica Microsystems) to acquire fluorescence data. Regions of interest (ROIs) were identified based on fluorescence signals indicative of intracellular iron and ROS accumulation. The identified ROIs were subsequently imaged using a Titan Krios microscope (Thermo Fisher Scientific), operated at 300 kV with a Gatan K3 detector. Two-dimensional (2D) search maps were acquired at a magnification of 4,800×. For tomographic data collection, a magnification of 8,700× was used, corresponding to a pixel size of 10.51 Å. The total electron dose was 27.53e^{-}/Å^{2}. Tilt series were acquired

from +60° to −60° in 3° increments, with a defocus value of −25 µm. Tomograms were reconstructed using the IMOD software package (University of Colorado, Boulder, CO). Microscopy Image Browser and ChimeraX were employed for volume segmentation and visualization of tomograms (19, 20).

From 2D search maps, several parameters were measured using Fiji (ImageJ) software, including cell length (n = 50 cells per condition), number of magnetosomes per cell (n = 50 cells per condition), percentage of area occupied by PHA granules relative to the total cell surface area (n = 20 cells per condition), and magnetite crystal size (n = 500 crystals per condition).

RESULTS AND DISCUSSION

MSR-1 physiological responses to stress conditions

To evaluate the physiological responses of MSR-1 to externally induced oxidative stress, the cells were exposed to H_2O_2 and iron citrate mid-growth. The physiological impact of these stressors was assessed through measurements of various parameters, such as cellular growth, cell viability, cell morphology and size, PHA formation, and ROS accumulation.

MSR-1 growth and viability

MSR-1 was grown under microaerobic and aerobic conditions to obtain magnetosome-producing cells and non-magnetosome-producing cells, respectively; these terms are used consistently throughout the manuscript. When the bacterial cells reached the early exponential growth phase ($OD_{565} \simeq 0.15$), a pulse of iron citrate (400 µM) or H_2O_2 (150 µM) was introduced to induce oxidative stress. The concentrations of iron citrate and H_2O_2 used in this experiment were selected based on literature data (11, 13, 21–23) and H_2O_2 tolerance tests performed on MSR-1 (Fig. S1).

Bacterial growth and cell viability were monitored over a period of 60 h. In microaerobic cultures, the addition of iron citrate did not impact bacterial growth (Fig. 1A) or cell viability (Fig. 1B). The extracellular iron concentration increased from 6 mg/L to approximately 20 mg/L following the iron citrate pulse (Fig. S2). Although previous work suggests that a 20 mg/L concentration should be toxic for MSR-1 (22, 23), our findings reported in another published study (24), and again herein, indicate that neither bacterial growth nor cell viability was affected by the increase in the extracellular iron concentration (across the studied concentration range up to 55 mg/L; Fig. S3A). In contrast, although bacterial growth in aerobic cultures remained unaffected by the addition of iron citrate (Fig. 1A), cell viability declined more rapidly compared with control conditions (Fig. 1B). This accelerated decline is tentatively attributed to potential cellular damage caused by the Fenton reaction (10).

On the other hand, the addition of H_2O_2 significantly impacted bacterial growth (Fig. 1A). Aerobic growth was completely ceased as the OD_{565} values dropped from 0.19 to 0.13, likely due to cell lysis. Meanwhile, the growth rate under microaerobic conditions was reduced but not completely restrained (OD_{565} = 0.22), relative to the control (OD_{565} = 0.37). Aerobic cultures also exhibited a much steeper decline in cell viability (Fig. 1B), with viability dropping from 85% to less than 10% immediately after the H_2O_2 pulse, whereas microaerobic cultures only decreased by 25% relative to the control. These effects can be attributed to the interaction of H_2O_2 with the bacterial cell membrane, which can cause lipid peroxidation and disrupt membrane integrity (25, 26). Oxidative stress can also reduce proton motive force by inhibiting transport across the cell membrane, which reduces ATP production and consequently inhibits cell growth, leading to cell death (27).

There are only a few studies published on the impact of H_2O_2 on MTB growth. The majority of which were performed under microaerobic conditions solely and started to see a significant impact on bacterial growth at 200–300 µM concentrations in the media (11, 13, 21). These studies typically exposed bacteria to different H_2O_2 concentrations

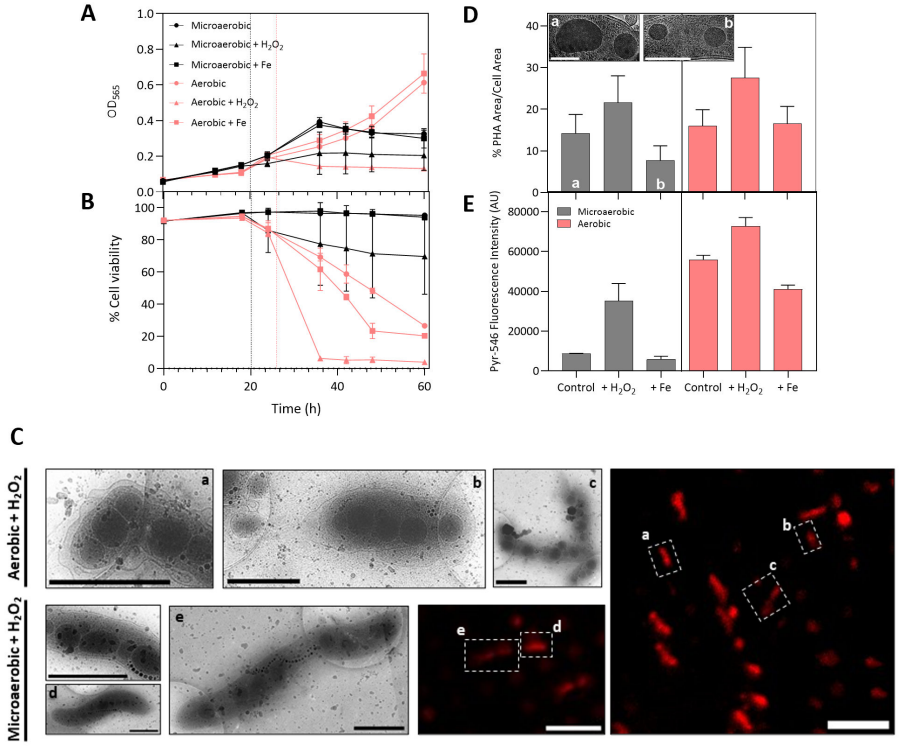

FIG 1 Effects of iron citrate and H_2O_2 addition on the physiology of MSR-1 cells grown under microaerobic and aerobic conditions. (A) Time course of cell growth. (B) Cell viability over time, determined by FCM. Vertical lines in graphs A and B indicate the addition of iron and H_2O_2 pulses in microaerobic (black) and aerobic (red) cultures. (C) CryoEM images of MSR-1 cells grown under aerobic and microaerobic conditions after the addition of H_2O_2 (~150 µM). The cryo-fluorescence image shows cells exposed to H_2O_2, incubated with the CellROX Deep Red fluorophore, which detects the presence of reactive oxygen species (ROS). The areas labeled (A-E) in the cryo-fluorescence image correspond to the cells highlighted in the cryoEM images with the same labels. Scale bar = 1 µm (cryoEM) and 10 µm (cryo-fluorescence). (D) Percentage of PHA area relative to the total cell area, measured from cryoEM images of MSR-1 cells collected at t = 36 h during the exponential growth phase (*n* = 20 cells/condition). Statistical analysis for this panel was performed using one-way ANOVA, followed by Tukey's post-hoc test; full results are provided in Table S2. Inset cryoEM images: (a) microaerobic condition and (b) microaerobic condition with iron addition. Scale bar = 300 nm. (E) Analysis of PHA content by FCM using Pyr-546 fluorophore at t = 36 h during the exponential growth phase; 25,000 events were analyzed per sample by FCM. Error bars represent the standard deviation of triplicates. FCM = Flow Cytometry; CryoEM = cryo-electron microscopy; Pyr-546 = Pyrromethene-546.

from the start of the culture, whereas our study introduces a pulse of H_2O_2 during mid-growth, which may explain the differences in the observed behavior. By introducing H_2O_2 as a pulse during mid-growth, this study specifically focuses on the physiological responses of MSR-1 to sudden oxidative perturbations, providing insight into how cells cope with acute stress rather than long-term adaptation. Under these conditions, microaerobic cells tolerated the iron pulse without affecting growth or viability and were lightly impacted by H_2O_2, whereas aerobic cells showed decreased viability with iron and were severely affected by H_2O_2 exposure.

MSR-1 cell size and morphology

The impact of external oxidative stress on MSR-1 cell morphology and size was analyzed, with a focus on the changes induced by doping high iron and H_2O_2 concentrations. FCM analysis provides insights into cell size and granularity, whereas cryo-electron microscopy (cryoEM) images offer high-resolution details of cellular structures. Together, these methodologies reveal the extent to which oxidative stress affects MSR-1 cells,

highlighting differences in their structural and intracellular organization. Samples for most analyses were collected every 6–12 h to monitor temporal dynamics; however, cryoEM was performed during the exponential growth phase (only at t = 36 h) to capture the full effects of the stress factors before the stationary phase or cell death.

The obtained results indicate that the addition of iron does not result in any noticeable morphological differences when grown under microaerobic or aerobic conditions. In contrast, as shown in Fig. 1C, H_2O_2 doping induces various effects on MSR-1 morphology. Aerobic cells subjected to H_2O_2 exhibited significantly more structural cell damage compared with microaerobic cells. The cell membrane of aerobic cells was notably compromised, with many cells losing their characteristic spirillum shape and becoming smaller and more rounded (Video S1). Some cells also appeared to be broken. Although some damage was observed in microaerobic cells exposed to H_2O_2, it was considerably less severe compared with the damage seen in aerobic conditions. This difference in structural cellular damage correlates with the larger decrease in cell viability observed in Fig. 1B under H_2O_2-doped aerobic conditions, where viability was reduced by 80%, compared with a 25% reduction in H_2O_2-doped microaerobic cultures. The sensitivity of bacterial cells to H_2O_2 has been documented in other bacterial species. For instance, *Campylobacter jejuni* changes from a spiral-shaped to a coccoid form upon interaction with ROS (28), whereas *Escherichia coli* turns from a bacillus form to a coccoid form (29). These morphological changes occur as bacteria attempt to repair the membrane damage caused by ROS, which, if unrepaired, may lead to DNA damage and cell death (30). Table 1 displays the differences in cell length under iron and H_2O_2 doping conditions, with cell length measured from cryoEM 2D search maps using Fiji software. The results revealed that exposure to H_2O_2 led to significantly shorter cells, about half the size of those in the control group, whereas iron exposure had no effect on cell size. This reduction in size is likely due to morphological changes caused by lipid peroxidation of the cell membrane from H_2O_2 exposure. Our findings also indicate that aerobic cells were significantly longer (8.3 ± 3.1 µm) than microaerobic cells (6.1 ± 1.8 µm) (one-way ANOVA with Tukey test, $P < 0.01$; Table S1). Some aerobic cells even reached double the size of some microaerobic cells, measuring up to 16 µm, which has also been previously observed by others (9). This difference in cell length can be clearly observed in Fig. S4, which shows representative aerobic and microaerobic cells. The analysis of the forward scatter (FSC-A) data from the FCM, which provides information regarding cell size, is in line with the microscopy results, showing that aerobic cells generally exhibited longer dimensions than microaerobic cells (Fig. S5A). In many bacteria, cell size is influenced by growth rate, but this relationship has not, to our knowledge, been systematically studied in MTB. Thus, although differences in oxygen and culture conditions may influence growth rate and thereby cell size, we cannot confirm that the same growth - rate/size rules apply to MSR-1. Besides oxygen availability, other changes in the growth conditions or other stress factors, such as variations in lactic acid and nitrate concentrations in the media (18), the method of cultivation (plates *vs*. liquid cultures) (31), or exposure to UV-B radiation (32), have been shown to affect the size and morphology of MTB. Monitoring and controlling cell size is therefore important, as this phenotypic feature can significantly impact bioprocess efficiency, influencing both upstream factors like nutrient uptake and downstream processes such as cell disruption and product recovery (33).

TABLE 1 Effects of doping iron citrate and H_2O_2 on cell length (*n*=50/condition), magnetosome content (*n* = 50/condition), and magnetite crystal size (*n* = 500/condition) in microaerobic and aerobic MSR-1 cells[a]

	Cell length (µm)		Magnetosomes/cell		Magnetite size (nm)	
	Microaerobic	Aerobic	Microaerobic	Aerobic	Microaerobic	Aerobic
Control	6.1 ± 1.8	8.3 ± 3.1	24.6 ± 5.5	11.8 ± 7.9	48.6 ± 10.5	34.5 ± 9.4
H_2O_2 addition	3.7 ± 1.8	4.5 ± 1.8	20.7 ± 7.2	8.0 ± 4.7	43.4 ± 10.6	43.1 ± 10.7
Iron addition	5.9 ± 1.0	7.5 ± 2.1	31.8 ± 7.0	8.4 ± 5.0	48.2 ± 11.4	35.0 ± 8.1

[a]All measurements were obtained from cryoEM 2D search maps using Fiji software. Statistical analysis details (one-way ANOVA followed by Tukey's post-hoc test) are provided in Tables S1, S3, and S4.

PHA granule accumulation

FCM was also used to assess intracellular complexity or granularity through side scatter (SSC-A) measurements. In MSR-1, aside from magnetosome chains, cells typically accumulate intracellular inclusions such as phosphate or PHA granules (34).

As is well known, PHA synthesis is notably enhanced under conditions of nutrient deficiency or oxidative stress, particularly when there is an excess of carbon source (35). Monitoring PHA synthesis is important because PHAs serve as reservoirs for reducing power, thereby helping us to manage intracellular redox balance and mitigate ROS formation (35), and their accumulation can function as an indirect indicator of cellular stress. By sequestering reducing equivalents (e.g., NADH and NADPH), PHA synthesis prevents excess reducing agents from fueling uncontrolled ROS production and oxidative damage (36). During periods of starvation, PHAs can be degraded to release monomers that enter central metabolic pathways (e.g., the TCA cycle and glycolysis), thereby restoring reducing power necessary for maintaining redox balance (37).

Here, PHA granules were stained with the Pyr-546 fluorophore and monitored by FCM. Changes in cell granularity (SSC-A) and Pyr-546 intensity values over time are shown in Fig. S5B and C**,** respectively. Both plots clearly indicate that aerobic conditions exhibited higher fluorescence and SSC-A values, suggesting increased PHA granule synthesis under these conditions. Our results are in accordance with the investigation of Su *et al*. using the AMB-1 strain in which they observed a decrease in PHA content under anaerobic conditions and an increase under aerobic conditions (38).

Figure 1D and E display the percentage of PHA inclusions in the cytoplasmic space and Pyr-546 fluorescence intensity values, respectively, for MSR-1 cells during the exponential growth phase, when samples were collected for cryoEM imaging. Both analytical approaches (FCM and cryo-EM) showed similar trends in PHA content across the different conditions. Under aerobic conditions, iron addition did not result in significant differences in PHA content as cells exhibited similar values to the control conditions (16% PHA area/cell area). However, under microaerobic conditions, the PHA area relative to total cell area decreased significantly from 14% to 8% with iron addition (one-way ANOVA with Tukey test, $P < 0.01$; Table S2). Inset cryo-EM images in Fig. 1D further show that the size of PHA granules was significantly reduced after iron addition under microaerobic conditions. Interestingly, in other bacterial species, such as *Methylobacterium extorquens*, a byproduct of PHA degradation (methyl-esterified 3-hydroxybutyrate) has been shown to exhibit powerful antioxidative activity against hydroxyl radicals (39). Although this mechanism has not been demonstrated in MSR-1, it highlights the possibility that PHA's metabolism may contribute more broadly to oxidative stress mitigation in MTB. In other bacterial species, such as *Cupriavidus necator*, the synthesis of PHA has been shown to increase under moderately elevated levels of oxidative stress (≤10 mM H_2O_2) (40, 41), supporting the notion that PHA accumulation can be part of a general stress response. In our study, the higher PHA content observed in H_2O_2-exposed cells (22% and 28% for microaerobic and aerobic cultures, respectively) may reflect a similar cellular response to oxidative stress or, alternatively, be biased by the changes in cell size and morphology resulting from H_2O_2-induced cell damage. For instance, broken cells had cytoplasmic leakage, reducing the total cell area and thereby increasing the ratio of PHA to cytoplasmic space, due to the cell damage rather than increased PHA production.

Monitoring PHA formation is important in bioprocessing since its accumulation reflects cellular stress and signals changes in culture physiology. Excessive PHA can divert carbon and reducing power away from magnetosome biosynthesis (18), lowering yields, whereas residual granules complicate downstream purification and reduce final product quality (42). Incorporating PHA monitoring into process control strategies can therefore enhance both culture performance and magnetosome recovery. This study provides one of the few assessments of PHA dynamics in MTB, revealing condition-dependent variations linked to environmental stress factors. These insights expand our understand-

ing of PHA physiology in MTB and underscore the need for further studies to elucidate the environmental and metabolic triggers that regulate their formation.

Intracellular ROS accumulation

MSR-1 cells were stained with CellROX Deep Red (CRDR) fluorophore and analyzed by FCM to investigate the accumulation of ROS. This fluorescent probe has been effectively employed for ROS detection in other gram-negative bacteria such as *Escherichia coli* (43) and *Fusobacterium nucleatum* (44).

Figure 2A illustrates ROS accumulation of MSR-1 cells exposed to oxidative stress conditions over time. Generally, cells under aerobic conditions exhibited significantly higher levels of intracellular ROS compared with those under microaerobic conditions. In microaerobic cultures, the addition of iron did not lead to an increase in ROS production. This was consistent with complementary experiments in which MSR-1 cells were grown with varying iron concentrations (up to 1 mM), as shown in Fig. S3B. In previous work, gene expression analysis performed during cell growth and magnetosome synthesis revealed that genes associated with ferric reductases, ferrous transport system, and ROS scavenging are highly expressed when exposed to high iron concentrations (45). The upregulation of ROS scavenging-related genes under high iron concentrations presumably facilitates the ability of MTB to uptake large amounts of iron and thrive in iron-rich environments. However, under aerobic conditions, ROS production spiked 22 h after cells were exposed to an iron pulse, most likely as a result of the Fenton reaction.

The addition of H_2O_2 resulted in a moderate increase in ROS accumulation for microaerobic conditions compared with the control (Fig. 2A and 1C). Surprisingly, H_2O_2-aerobic cultures exhibited lower CRDR fluorescence values compared with the control conditions when analyzed by FCM. However, fluorescence microscopy images (insets in Fig. 2A) revealed similar fluorescence levels to those achieved in aerobic control conditions. Aerobic cells were significantly damaged under the influence of H_2O_2, resulting in smaller, more compact, and even fragmented cells (Fig. 1C). This loss of membrane integrity likely led to partial leakage of the CRDR dye, which can cause an apparent decrease in fluorescence intensity detected by FCM (46). Nevertheless, microscopy still revealed strong fluorescence within the damaged cells, consistent with high intracellular ROS levels. This complementary interpretation underscores the value of combining FCM and fluorescence imaging to better capture cellular responses under stress conditions.

Using the gating capability of FCM, a more in-depth analysis of ROS distribution was conducted by comparing low magnetosome-producing cells (aerobic) with high magnetosome-producing cells (microaerobic), as magnetosomes are believed to decrease and eliminate ROS due to their peroxidase-like activity (14). Analysis of the proportion of CRDR-stained cells (ROS^+) in Fig. 2B revealed a 20% difference between these two conditions, with 55% of ROS^+-microaerobic cells compared with 75% ROS^+-aerobic cells. ROS^+ cells were defined based on fluorescence above the threshold set using non-stained control samples, indicating the presence of ROS. A closer examination of the mean fluorescence intensity values of ROS^+ cells (Fig. 2C) reveals that ROS^+-aerobic cells showed double the fluorescence compared with ROS^+-microaerobic cells, indicating a clear contrast in ROS levels between the two conditions. Importantly, no correlation was observed between FSC-A and CRDR fluorescence intensity (Fig. S6), confirming that the observed differences in fluorescence are not attributable to cell size but rather reflect physiological differences in ROS accumulation between conditions.

Based on FSC-A and SSC-A plots, two distinct populations can be identified for both microaerobic and aerobic conditions (Fig. S7A). The first population (P1) consists of smaller cells with fewer granules, constituting approximately 70% of the total cell population, whereas the second population (P2) consists of larger cells with higher granule content, representing the remaining 30%. Both aerobic populations also exhibited a much higher percentage of ROS^+ cells (P1: 70%; P2: 90%) compared with microaerobic populations (P1: 45%; P2: 70%) (Fig. S7B). A similar trend to the one previously observed is clear, with aerobic populations displaying at least twice the level

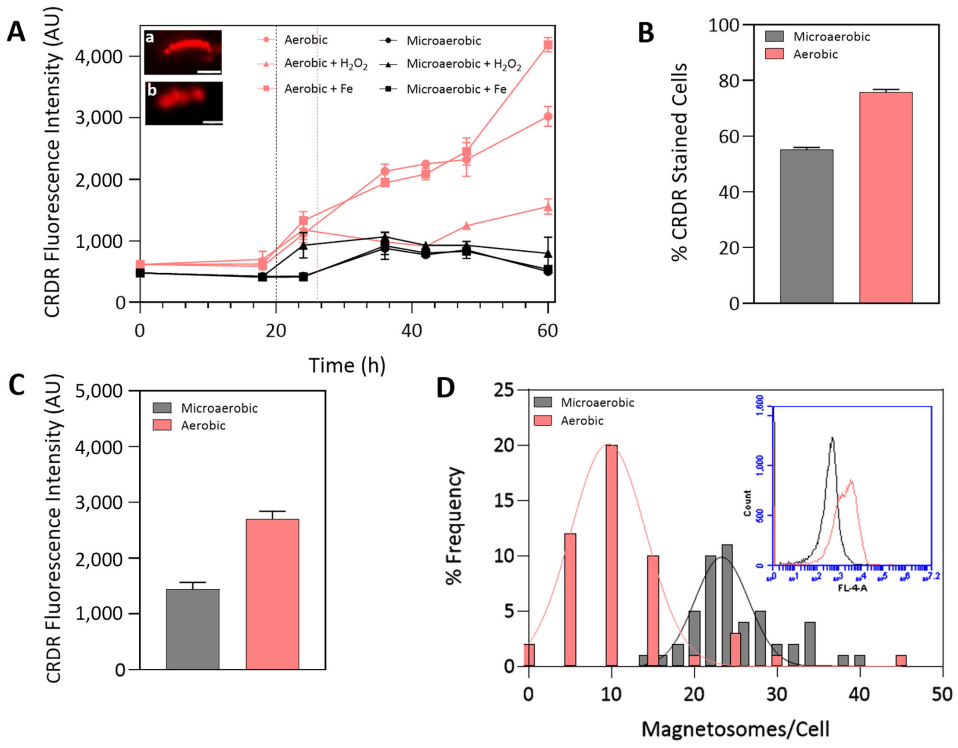

FIG 2 (A) Accumulation of ROS in CRDR-stained MSR-1 cells by FCM. Inset cryo-fluorescence images: (a) aerobic control condition and (b) aerobic condition with H_2O_2 addition. Scale bar = 2 µm. Comparison between aerobic and microaerobic MSR-1 cells of (B) the percentage of CRDR-stained cells and (C) the fluorescence intensity values of the CRDR-stained cells during the exponential growth phase (t = 36 h). (D) Magnetosome chain length histogram distribution of aerobic and microaerobic cells. The inset graph corresponds to CRDR fluorescence histograms obtained from FCM analysis of aerobic and microaerobic cells. Vertical lines in graph (A) indicate the addition of iron and H_2O_2 pulses in microaerobic (black) and aerobic (red) cultures; 25,000 events were analyzed per sample by FCM. Error bars represent the standard deviation of triplicates. CRDR = CellROX Deep Red; FCM = Flow cytometry; AU = arbitrary units.

of fluorescence compared with microaerobic populations (Fig. S7C). It is also noteworthy to mention that the difference in fluorescence values between P1 and P2 under microaerobic conditions is only 1.6-fold, whereas under aerobic conditions, it is 2.2-fold. This indicates that magnetosome-producing cells (microaerobic) display both lower fluorescence heterogeneity and lower ROS levels compared with non-magnetosome-producing cells (aerobic). This fluorescence heterogeneity is also reflected in the FCM fluorescence histograms (Fig. 2D inset). The CRDR fluorescence peak observed in the CRDR histograms for microaerobic cells was narrower compared with the broader distribution observed for aerobic cells. This pattern was in line with the magnetosome chain length distribution plots for both conditions (Fig. 2D), where the distribution of magnetosome chain lengths in aerobic cells was much more dispersed than in microaerobic cells. The aerobic distribution has a coefficient of variation (CV) of 135%, indicating higher relative dispersion compared with the microaerobic distribution, which has a CV of 96%. This suggests that the higher CRDR fluorescence heterogeneity observed in aerobic conditions is potentially correlated with greater heterogeneity in magnetosome content. Considering that prior studies have demonstrated that MSR-1 mutants deficient in magnetosome production exhibit significantly higher ROS levels than the wild-type strain capable of producing magnetosomes, even when both were grown under microaerobic conditions (14), our findings are consistent with a potential correlation between the heterogeneity in magnetosome content and ROS levels, as reflected by the observed fluorescence heterogeneity. Although the functional

implications of this fluorescence heterogeneity remain unclear, its consistent association with both ROS levels and magnetosome content in our observations and in previous reports suggests that it reflects underlying physiological regulation in MSR-1 and should be the focus of future investigations.

Impact of stress conditions on magnetosome biomineralization

The regulation of iron homeostasis is intrinsically linked with the bacterial response to oxidative stress, reflecting a coordinated control system to manage these demands (47). In MTB, this coordination is particularly crucial, as iron is a key component in magnetosome biomineralization. In here, the impact of stress conditions on magnetosome formation in magnetosome-producing and non-magnetosome-producing MSR-1 cells is further explored. Understanding these interactions and regulatory mechanisms is vital for elucidating how MTB manage iron homeostasis while minimizing oxidative damage. Thus, it is of special interest to improve current bioprocessing strategies.

Magnetosome chain length, morphology, and crystal size

Changes in the culture media and external environmental factors, such as temperature, pH, dissolved oxygen levels, and iron concentrations can affect the number and shape of the magnetosome crystals (4, 48–50). In this study, the impact of adding H_2O_2 and iron citrate on magnetosome content, chain morphology, and crystal size was analyzed using cryoEM (Table 1).

Despite the suppression of magnetosome biomineralization under aerobic conditions (9), magnetosome chains were still present due to the high magnetism of the inoculum used (C_{mag} = 2.7, Video S2). However, as displayed in Table 1, the chains in aerobic cells were only half as long (11.8 ± 7.9 magnetosomes/cell) as those in microaerobic cells (24.6 ± 5.5 magnetosomes/cell) (Video S3). The addition of iron and H_2O_2 to aerobic cells did not significantly alter the number of magnetosomes per cell. In contrast, under microaerobic conditions, the iron pulse resulted in the formation of significantly (one-way ANOVA with Tukey test, $P < 0.01$; Table S3) longer magnetosome chains (31.8 ± 2.1 magnetosomes/cell). These findings align with our previously published study, which demonstrated that increasing extracellular iron content promotes the formation of longer magnetosome chains (24).

As shown in Fig. 3A, the spacing between magnetite crystals in aerobic cells was larger compared with microaerobic cells (9). Although the addition of iron did not induce any noticeable changes in magnetosome chain morphology, the exposure to H_2O_2 affected the chain structure. The oxidative stress induced by H_2O_2 led to the loss or deformation of the typical needle-like shape and, in some cases, caused chain fragmentation. MamK is an actin-like protein responsible for organizing the magnetosome chain along the cell axis (51). Similar to what has been observed in eukaryotic cells, where H_2O_2 disrupts actin dynamics [25], oxidative stress from H_2O_2 could have impaired the function of MamK, leading to the observed structural alterations.

Measurement of magnetite crystal size under the different culture conditions (Table 1) from 2D cryoEM search maps revealed that microaerobic magnetosomes were significantly larger (48.6 ± 10.5 nm) than those present in aerobic cells (34.5 ± 9.4 nm) (one-way ANOVA with Tukey test, $P < 0.01$; Table S4) (52). Iron addition did not enlarge magnetosome crystals under microaerobic conditions, but H_2O_2 exposure resulted in significantly smaller crystals. This reduction in magnetite crystal size caused by H_2O_2 is consistent with previous studies in which MSR-1 cells were exposed to similar H_2O_2 concentrations (200 µM) (53). Although other research has reported a correlation between increased extracellular iron concentration and larger magnetite crystals in the AMB-1 strain (54), our results did not show an increase in magnetite size upon iron addition (48.2 ± 11.4 nm). This discrepancy may be due to differences in experimental protocols, as bacteria were grown at different iron concentrations from the start, whereas in this study, the iron pulse was added mid-growth, potentially affecting magnetite growth differently. Other studies have reported that increasing extracellular iron concentration can alter the

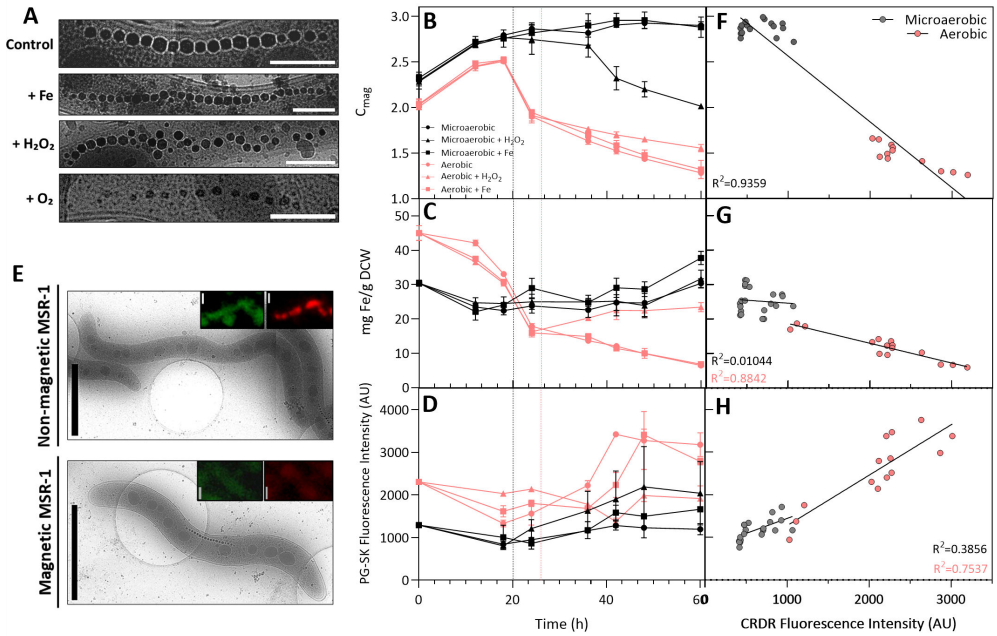

FIG 3 Analysis of iron dynamics and ROS accumulation during magnetosome biomineralization. (A) Effects of the addition of iron citrate (+ Fe), hydrogen peroxide (+ H_2O_2), or aerobic conditions (+ O_2) on the magnetosome chain structure. Scale bar = 300 nm. (B) C_{mag}, (C) total intracellular iron content, and (D) labile ferrous iron levels in MSR-1 cells grown under various stress conditions over a period of 60 h. Vertical lines in (B-D) indicate the addition of iron and H_2O_2 pulses in microaerobic (black) and aerobic (red) cultures. (E) Comparison between non-magnetic (aerobic) and magnetic (microaerobic) MSR-1 cells using PG-SK and CRDR fluorescence, alongside their corresponding cryoEM images. Scale bar = 2 µm. (F-H) Correlation of C_{mag} (*n*=30), total intracellular iron content (*n*=36), and labile ferrous iron levels (*n*=35) with intracellular ROS accumulation of microaerobic and aerobic cells, respectively. Each data point in (F–H) corresponds to the same measurements shown in (B–D), but only for the control aerobic and microaerobic conditions. Labile ferrous iron levels and ROS accumulation were measured using (D-H) flow cytometry (FCM) or (E) cryo-fluorescence microscopy with PG-SK (green fluorescence) and CRDR (red fluorescence) fluorophores, respectively; 25,000 events were analyzed per sample by FCM. Error bars represent the standard deviation of triplicates. CRDR = CellROX Deep Red; PG-SK = PhenGreen SK; AU = arbitrary units.

morphology of magnetosome crystals rather than their size when iron uptake rates are affected (48). Specifically, magnetosomes grown under high iron uptake rates displayed cuboidal morphologies, whereas those grown with slower iron uptake rates exhibited the classical cubo-octahedral morphology. These observations highlight the complexity of magnetosome biomineralization and emphasize the critical role of environmental factors in shaping magnetosome morphology. Beyond these individual effects, our findings underline that the physiological and phenotypic responses involved are interconnected and cannot be fully understood in isolation. By combining complementary approaches, this study provides a holistic view of magnetosome formation as a multifactorial process governed by both environmental and intracellular parameters, advancing our understanding of biomineralization within its broader physiological context rather than through isolated variables.

Interplay between iron content and ROS accumulation

Figure 3B shows C_{mag} values recorded at regular intervals to enable in-line analysis of magnetosome content over time. The determination of the number of magnetosomes per cell by cryoEM was conducted at a single time point (during the exponential growth phase, t = 36 h); thus, the collection of C_{mag} values ensured a more continuous assessment of magnetosome content, complementing the cryoEM data. As aforementioned, the inoculum used was highly magnetic; hence, C_{mag} values for microaerobic

conditions were consistently high from the beginning and maintained throughout the experiment (C_{mag} = 2.3–2.9). For aerobic cultures, there was a period of adaptation of approximately 20 h in which cells switched to their aerobic metabolism. Afterward, C_{mag} values began to decrease, down to 1.3, indicating the suppression of magnetosome production (9, 18). There were practically no C_{mag} differences between the control and the iron-doping conditions for both microaerobic and aerobic conditions. Notably, differences in C_{mag} values were only observed in conditions where H_2O_2 was added (Fig. 3B). These observations showed some inconsistencies with the cryoEM magnetosome content results displayed in Table 1, where no significant differences in magnetosome content were found upon H_2O_2 addition. Although cryoEM provides precise, high-resolution information on cell morphology and the exact number of magnetosomes per cell, it is an offline, low-throughput technique. In contrast, C_{mag} offers a rapid, in-line, and qualitative assessment of culture's magnetism, although its values can be influenced by factors such as cell length and morphology (31). The discrepancies observed under H_2O_2 stress are therefore likely explained by morphology-dependent effects on C_{mag}, whereas cryoEM more accurately reflected the actual number of magnetosomes per cell at the measured time point. Together, the two methods provide complementary perspectives on the impact of stress on MSR-1 cells.

Total intracellular iron content results (Fig. 3C) followed a trend similar to that observed in the C_{mag} results. In aerobic cultures, the iron concentration decreased up to 7 mg/g DCW, whereas in microaerobic cultures, the iron concentration remained consistently high, around 30 mg/g DCW over time (9, 52). Unlike C_{mag} data, microaerobic conditions with added iron displayed higher intracellular iron concentrations (38 mg/g DCW), likely due to the presence of longer magnetosome chains (Table 1). After H_2O_2 addition in aerobic conditions, the intracellular iron levels remained constant. This was attributed to the cease of cell growth and significant cell viability reduction (Fig. 1) that these cells suffered under these conditions.

Measurement of the total intracellular iron content has been commonly used to assess magnetosome content. However, as noted in previous studies, there are different intracellular iron pools distinct from magnetite (24, 55, 56). In addition to its role in magnetite biomineralization, iron is also required for other general iron-dependent biochemical reactions (57, 58) or stored in proteins such as ferritins to prevent toxicity (59). Consequently, some studies have suggested that only a fraction of the total intracellular iron (25%–45%) corresponds to magnetite (55, 56). Hence, the importance of also tracking changes of the soluble Fe^{2+} intracellular iron pool. This is particularly important because free iron (Fe^{2+}) can react with H_2O_2 to generate hydroxyl radicals.

Labile Fe^{2+} intracellular iron concentration was monitored by FCM using PG-SK fluorophore, which quenches upon binding to free Fe^{2+} ions (31, 60). As shown in Fig. 3D, aerobic cultures displayed higher green fluorescence values compared with microaerobic cultures, indicating a notably lower presence of Fe^{2+} under aerobic conditions. This observation was corroborated by cryo-fluorescence microscopy, as shown in Fig. 3E. Under microaerobic conditions, the addition of H_2O_2 led to a decrease in Fe^{2+} levels. This decrease was likely due to oxidation of Fe^{2+} to Fe^{3+} via the Fenton reaction, as ROS levels also increased (Fig. 2A).

In a previous correlative microscopy study (24), we found a direct correlation between the number of magnetosomes and the intracellular Fe^{2+} iron pool, in which cells with longer magnetosome chains exhibited higher Fe^{2+} levels than those with shorter chains. It also showed that not all internalized Fe^{2+} was used for magnetite synthesis, as a substantial labile Fe^{2+} pool remained even after biomineralization was complete (61). Given these observations, in this study, we aimed to elucidate the relationship between ROS accumulation, the intracellular soluble iron pool, and magnetosome content. To this end, C_{mag} values (Fig. 3F), total intracellular iron content (Fig. 3G), and intracellular Fe^{2+} levels (Fig. 3H) were correlated with ROS accumulation. Additionally, the cryoCLEM approach was employed to obtain data at the single-cell level (Fig. 3E and 4) by comparing magnetic (microaerobic) and non-magnetic (aerobic) cells.

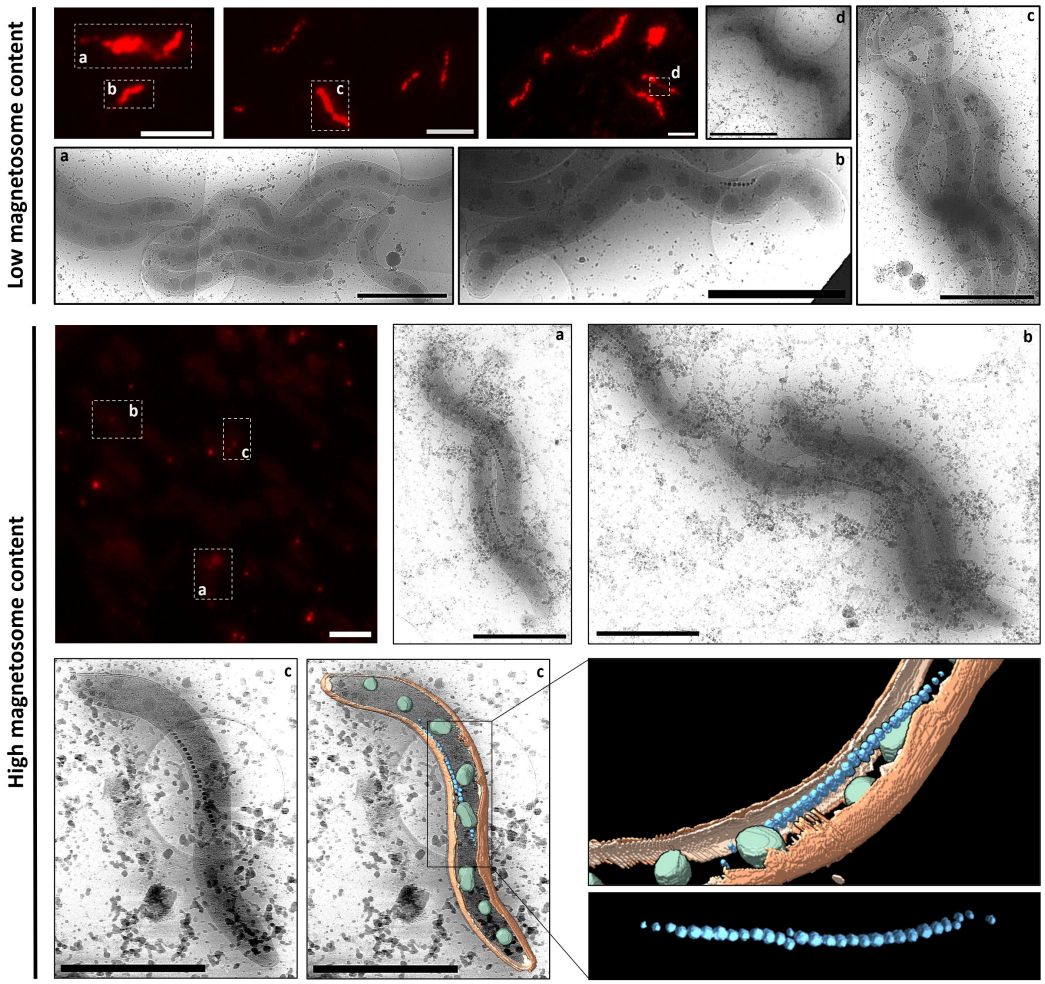

FIG 4 Comparison of intracellular ROS accumulation of MSR-1 cells containing high or low magnetosome content. Cells were stained with CellROX Deep Red fluorophore to detect ROS presence. CryoEM images of selected cells are matched to the corresponding cryo-fluorescence images as indicated by the same letter labels. A representative 3D volumetric representation of a highly magnetic cell is included. Magnetosome chain is colored in blue, PHA granules in green, outer membrane in orange, and inner membrane in light orange (Video S4). Scale bar = 2 µm (cryoEM) and 10 µm (cryofluorescence).

Evidence suggests that MSR-1 possesses homologs for the global regulators Fur (62), OxyR (21), and IrrB (63), indicating that these regulators work together to fine-tune iron homeostasis and oxidative stress responses during magnetosome biomineralization. In MSR-1, Fur is involved in regulating the transcription of Fe^{2+} transport systems *feoAB1* and *feoAB2*, as well as genes involved in oxidative stress responses, such as *katG* (catalase) and *sodB* (superoxide dismutase) (62, 64). This highlights Fur's dual role in managing both iron levels and oxidative stress. OxyR, a key regulator of the oxidative stress response, responds to H_2O_2 by upregulating genes that mitigate ROS damage such as *katG* and *dps* (iron storage protein) (65). Therefore, OxyR also indirectly influences iron metabolism by promoting iron sequestration and reducing free iron levels, thus helping in lower ROS formation (11). The combined actions of Fur and OxyR underscore the complex interplay between iron regulation and oxidative stress management.

Our results, shown in Fig. 3F, revealed an inverse correlation between C_{mag} values and ROS accumulation. Specifically, higher C_{mag} values, which indicate greater magnetosome content, were associated with lower ROS levels. This suggests that increased magnetosome formation might be linked to reduced oxidative stress, potentially due to iron sequestration within magnetite or their peroxidase-like activity (14). This trend is

further supported by single-cell correlative microscopy images presented in Fig. 4, where MSR-1 cells with higher magnetosome content exhibited lower CRDR fluorescence than cells with lower magnetosome content.

By analyzing the correlation between the total intracellular iron content and ROS levels (Fig. 3G), distinct patterns between microaerobic and aerobic conditions were observed. It was expected that, due to the Fenton reaction, cells with higher intracellular iron concentrations would exhibit elevated ROS levels, as excess iron can catalyze ROS formation. However, under microaerobic conditions, which exhibited high intracellular iron concentrations over time, did not show a significant correlation between total iron content and ROS accumulation, suggesting that MSR-1 cells may regulate intracellular iron in a way that prevents excessive ROS formation under microaerobic conditions. Such regulation could involve iron-storage proteins, such as bacterioferritins, which have been reported in MSR-1 and linked to oxidative stress responses rather than magnetosome biomineralization (59). Their expression is also regulated by the OxyR ROS regulator, further supporting a role in mitigating iron-induced oxidative stress (11). In contrast, in aerobic conditions, a decrease in total intracellular iron content corresponded with an increase in ROS levels. This may result from a reduction in the number of magnetosomes per cell, thereby diminishing the capacity of MSR-1 cells to mitigate oxidative stress through magnetosome-associated ROS scavenging activity (13, 14). Despite Fur acting directly as a global regulator responding to iron levels (66), oxidative stress (such as that caused by high oxygen conditions) can influence iron homeostasis and indirectly affect Fur activity. Cells might respond by more tightly regulating iron uptake and storage to minimize the availability of free iron that could participate in ROS generation. This response could hypothetically involve Fur-mediated pathways to ensure iron levels are kept within a safe range, although Fur's primary direct response is to iron rather than to ROS or oxygen levels (62).

The correlation between labile Fe^{2+} (detected by PG-SK fluorescence) and ROS levels also varied notably depending on oxygen availability (Fig. 3H). Under microaerobic conditions, no significant correlation was observed. However, under aerobic conditions, a clear inverse correlation was observed: lower Fe^{2+} levels, indicated by higher PG-SK fluorescence, were associated with increased ROS accumulation. This relationship can be explained by the Fenton reaction. Since PG-SK has a high affinity for Fe^{2+} but not for Fe^{3+} (67), its fluorescence increases as Fe^{2+} is oxidized and becomes less detectable by PG-SK, whereas ROS levels rise. Correlative microscopy images in Fig. 3E further illustrate this situation, showing that magnetic cells exhibited low PG-SK and CRDR fluorescence, whereas non-magnetic cells exhibited high fluorescence. The images shown are representative of the cell population, for which the same trends were consistently observed.

Overall, these results suggest that magnetosomes likely play a significant role in mitigating oxidative stress, but this role cannot be completely disentangled from the broader physiological effects of oxygen availability in the absence of magnetosome-deficient mutants. The observed correlations, therefore, reflect the complex interplay between antioxidant mechanisms, iron homeostasis, and magnetosome biomineralization. Even within this multifactorial context, the integrated analysis presented here expands our understanding of magnetosome physiology and emphasizes the importance of simultaneously monitoring these interconnected parameters to enhance both fundamental knowledge and bioprocess efficiency.

Conclusions

This study highlights the complexity of MSR-1 physiological responses, showing that phenotypic changes, including cell size and morphology, magnetosome formation, ROS and PHA accumulation, cell viability, and intracellular iron levels, are interconnected and influenced by multiple environmental stress factors such as oxygen availability, iron concentration, and oxidative stress. By specifically focusing on responses to sudden oxidative perturbations, this work provides insight into how cells cope with acute

stress rather than long-term adaptation. Our findings reveal distinct differences in how microaerobic magnetosome-producing and aerobic non-producing MSR-1 cells respond to sudden environmental changes. Under microaerobic conditions, cells were smaller, accumulated less PHAs, maintained high magnetosome and iron levels, and experienced minimal oxidative stress, whereas aerobic cells were larger, with reduced magnetosome and iron levels, accumulated more PHAs, increased ROS levels, and a significantly decreased viability. In line with previous reports on magnetosome-deficient mutants, our findings indicate that magnetosomes are likely to play an important role in mitigating oxidative stress, whereas oxygen concentration and related metabolic processes may also contribute to shaping ROS levels. This highlights the complex interplay between antioxidant mechanisms, iron regulation, and magnetosome biomineralization. By combining complementary high-resolution and high-throughput techniques (e.g., cryoCLEM, FCM, and ICP-OES) in a single integrated experimental design, this work provides a unique, multi-dimensional view of MTB responses. Beyond fundamental insights into MTB biology, these findings have practical implications for bioprocessing, as monitoring interconnected physiological parameters can improve culture robustness, magnetosome yield, and downstream processing efficiency. Overall, this work establishes a benchmark for future studies on MTB stress responses and underscores the value of integrated, correlative analytical approaches in revealing complex microbial physiology.

ACKNOWLEDGMENTS

This work was supported by the Royal Society Research Grant RGS\R1\191377, BBSRC New Investigators Award Grant No. BB/V010603/1, and the Energy Research Accelerator (ERA) grant from Innovate UK (project No. 160052). The Aston Institute for Membrane Excellence (AIME) is funded by UKRI's Research England as part of their Expanding Excellence in England (E3) fund.

The authors acknowledge Diamond Light Source for access and support of the cryoEM facilities at the UK national electron Bio-Imaging Centre (eBIC), proposal BI31371. MMM acknowledges Aston University for an EPSRC-DTP-funded PhD studentship.

AUTHOR AFFILIATIONS

[1]Energy and Bioproducts Research Institute, Aston University, Birmingham, United Kingdom
[2]Aston Institute for Membrane Excellence, Aston University, Birmingham, United Kingdom
[3]Electron Bio-Imaging Centre (eBIC), Diamond Light Source, Harwell Science and Innovation Campus, Didcot, United Kingdom

AUTHOR ORCIDs

Marta Masó-Martínez http://orcid.org/0000-0002-9982-483X
Alfred Fernández-Castané http://orcid.org/0000-0002-2572-7797

FUNDING

Funder	Grant(s)	Author(s)
Royal Society	RGS\R1\191377	Alfred Fernández-Castané
Innovate UK	160052	Alfred Fernández-Castané
UK Research and Innovation	Expanding Excellence in England (E3) - AIME	Paul D. Topham
Diamond Light Source	BI31371	Marta Masó Martínez Alfred Fernández-Castané
BBSRC	BB/V010603/1	Alfred Fernández-Castané

AUTHOR CONTRIBUTIONS

Marta Masó-Martínez, Conceptualization, Formal analysis, Funding acquisition, Investigation, Methodology, Visualization, Writing – original draft | Julika Radecke, Investigation, Writing – review and editing | Craig MacGregor-Chatwin, Investigation | Paul D. Topham, Supervision, Writing – review and editing | Alfred Fernández-Castané, Conceptualization, Funding acquisition, Resources, Supervision, Writing – review and editing

ADDITIONAL FILES

The following material is available online.

Supplemental Material

Supplemental material (mBio03265-25-s0001.docx). Supplemental figures, tables, and video captions.
Video S1 (mBio03265-25-s0002.avi). MSR-1 cryo-electron tomography showing the damaging effects of H2O2 exposition.
Video S2 (mBio03265-25-s0003.avi). Representative cryo-electron tomography of MSR-1 cells grown aerobically presenting low magnetosome content.
Video S3 (mBio03265-25-s0004.avi). Representative cryo-electron tomography of an MSR-1 cell grown under microaerobic conditions presenting high magnetosome content.
Video S4 (mBio03265-25-s0005.avi). Representative cryo-electron tomography and its 3D volumetric segmentation of an MSR-1 cell grown under microaerobic conditions presenting high magnetosome content.

REFERENCES

1. Wojtaszek P. 1997. Oxidative burst: an early plant response to pathogen infection. Biochem J 322 (Pt 3):681–692. https://doi.org/10.1042/bj3220681
2. Sen A, Imlay JA. 2021. How microbes defend themselves from incoming hydrogen peroxide. Front Immunol 12:667343. https://doi.org/10.3389/fimmu.2021.667343
3. Munna MS, Nur I, Rahman T, Noor R. 2013. Influence of exogenous oxidative stress on *Escherichia coli* cell growth, viability and morphology. AJBIO 1:59. https://doi.org/10.11648/j.ajbio.20130104.12
4. Faivre D, Schüler D. 2008. Magnetotactic bacteria and magnetosomes. Chem Rev 108:4875–4898. https://doi.org/10.1021/cr078258w
5. Gandia D, Gandarias L, Rodrigo I, Robles - García J, Das R, Garaio E, García JÁ, Phan M, Srikanth H, Orue I, Alonso J, Muela A, Fdez - Gubieda ML. 2019. Unlocking the potential of magnetotactic bacteria as magnetic hyperthermia agents. Small 15:1902626. https://doi.org/10.1002/smll.201902626
6. Felfoul O, Mohammadi M, Taherkhani S, de Lanauze D, Zhong Xu Y, Loghin D, Essa S, Jancik S, Houle D, Lafleur M, Gaboury L, Tabrizian M, Kaou N, Atkin M, Vuong T, Batist G, Beauchemin N, Radzioch D, Martel S. 2016. Magneto-aerotactic bacteria deliver drug-containing nanoliposomes to tumour hypoxic regions. Nat Nanotechnol 11:941–947. https://doi.org/10.1038/nnano.2016.137
7. Tanaka M, Knowles W, Brown R, Hondow N, Arakaki A, Baldwin S, Staniland S, Matsunaga T. 2016. Biomagnetic recovery and bioaccumulation of selenium granules in magnetotactic bacteria. Appl Environ Microbiol 82:3886–3891. https://doi.org/10.1128/AEM.00508-16
8. Zhang Y, Ni Q, Xu C, Wan B, Geng Y, Zheng G, Yang Z, Tao J, Zhao Y, Wen J, Zhang J, Wang S, Tang Y, Li Y, Zhang Q, Liu L, Teng Z, Lu G. 2019. Smart bacterial magnetic nanoparticles for tumor-targeting magnetic resonance imaging of HER2-positive breast cancers. ACS Appl Mater Interfaces 11:3654–3665. https://doi.org/10.1021/acsami.8b15838
9. Heyen U, Schüler D. 2003. Growth and magnetosome formation by microaerophilic *Magnetospirillum* strains in an oxygen-controlled fermentor. Appl Microbiol Biotechnol 61:536–544. https://doi.org/10.1007/s00253-002-1219-x
10. Halliwell B, Gutteridge JMC. 1984. Oxygen toxicity, oxygen radicals, transition metals and disease. Biochem J 219:1–14. https://doi.org/10.1042/bj2190001
11. Niu W, Zhang Y, Liu J, Wen T, Miao T, Basit A, Jiang W. 2020. OxyR controls magnetosome formation by regulating magnetosome island (MAI) genes, iron metabolism, and redox state. Free Radic Biol Med 161:272–282. https://doi.org/10.1016/j.freeradbiomed.2020.10.015
12. Zhang Y, Wen T, Guo F, Geng Y, Liu J, Peng T, Guan G, Tian J, Li Y, Li J, Ju J, Jiang W. 2017. The Disruption of an OxyR-like protein impairs intracellular magnetite biomineralization in *Magnetospirillum gryphiswaldense* MSR-1. Front Microbiol 08:241628. https://doi.org/10.3389/fmicb.2017.00208
13. Li K, Wang P, Chen C, Chen C, Li L, Song T. 2017. Light irradiation helps magnetotactic bacteria eliminate intracellular reactive oxygen species. Environ Microbiol 19:3638–3648. https://doi.org/10.1111/1462-2920.13864
14. Guo FF, Yang W, Jiang W, Geng S, Peng T, Li JL. 2012. Magnetosomes eliminate intracellular reactive oxygen species in *Magnetospirillum gryphiswaldense* MSR-1. Environ Microbiol 14:1722–1729. https://doi.org/10.1111/j.1462-2920.2012.02707.x
15. Woehl TJ, Kashyap S, Firlar E, Perez-Gonzalez T, Faivre D, Trubitsyn D, Bazylinski DA, Prozorov T. 2014. Correlative electron and fluorescence microscopy of magnetotactic bacteria in liquid: toward *in vivo* imaging. Sci Rep 4:6854. https://doi.org/10.1038/srep06854
16. Li J, Liu P, Menguy N, Benzerara K, Bai J, Zhao X, Leroy E, Zhang C, Zhang H, Liu J, Zhang R, Zhu K, Roberts AP, Pan Y. 2022. Identification of sulfate-reducing magnetotactic bacteria via a group-specific 16S rDNA primer and correlative fluorescence and electron microscopy: Strategy for culture-independent study. Environ Microbiol 24:5019–5038. https://doi.org/10.1111/1462-2920.16109
17. Li J, Zhang H, Menguy N, Benzerara K, Wang F, Lin X, Chen Z, Pan Y. 2017. Single-cell resolution of uncultured magnetotactic bacteria via fluorescence-coupled electron microscopy. Appl Environ Microbiol 83:1–16. https://doi.org/10.1128/AEM.00409-17
18. Fernández-Castané A, Li H, Thomas ORT, Overton TW. 2018. Development of a simple intensified fermentation strategy for growth of *Magnetospirillum gryphiswaldense* MSR-1: Physiological responses to

changing environmental conditions. N Biotechnol 46:22–30. https://doi.org/10.1016/j.nbt.2018.05.1201
19. Pettersen EF, Goddard TD, Huang CC, Meng EC, Couch GS, Croll TI, Morris JH, Ferrin TE. 2021. UCSF ChimeraX: Structure visualization for researchers, educators, and developers. Protein Sci 30:70–82. https://doi.org/10.1002/pro.3943
20. Belevich I, Joensuu M, Kumar D, Vihinen H, Jokitalo E. 2016. Microscopy image browser: a platform for segmentation and analysis of multidimensional datasets. PLoS Biol 14:e1002340. https://doi.org/10.1371/journal.pbio.1002340
21. Ma Y, Guo F, Zhang Y, Sun X, Wen T, Jiang W. 2021. OxyR-like improves cell hydrogen peroxide tolerance by participating in monocyte chemotaxis and oxidative phosphorylation regulation in *Magnetospirillum gryphiswaldense* MSR-1. J Biomed Nanotechnol 17:2466–2476. https://doi.org/10.1166/jbn.2021.3205
22. Schüler D, Baeuerlein E. 1996. Iron-limited growth and kinetics of iron uptake in *Magnetospirillum gryphiswaldense*. Arch Microbiol 166:301–307. https://doi.org/10.1007/s002030050387
23. Hatami-Giklou Jajan L, Hosseini SN, Ghorbani M, Mousavi SF, Ghareyazie B, Abolhassani M. 2019. Effects of environmental conditions on high-yield magnetosome production by *Magnetospirillum gryphiswaldense* MSR-1. ibj 23:209–219. https://doi.org/10.29252/ibj.23.3.209
24. Masó-Martínez M, Bond J, Okolo CA, Jadhav AC, Harkiolaki M, Topham PD, Fernández-Castané A. 2024. An integrated approach to elucidate the interplay between iron uptake dynamics and magnetosome formation at the single-cell level in *Magnetospirillum gryphiswaldense* ACS Appl Mater Interfaces 16:62557–62570. https://doi.org/10.1021/acsami.4c15975
25. Maness PC, Smolinski S, Blake DM, Huang Z, Wolfrum EJ, Jacoby WA. 1999. Bactericidal activity of photocatalytic TiO(2) reaction: toward an understanding of its killing mechanism. Appl Environ Microbiol 65:4094–4098. https://doi.org/10.1128/AEM.65.9.4094-4098.1999
26. Hong Y, Zeng J, Wang X, Drlica K, Zhao X. 2019. Post-stress bacterial cell death mediated by reactive oxygen species. Proc Natl Acad Sci USA 116:10064–10071. https://doi.org/10.1073/pnas.1901730116
27. Farr SB, Touati D, Kogoma T. 1988. Effects of oxygen stress on membrane functions in *Escherichia coli*: role of HPI catalase. J Bacteriol 170:1837–1842. https://doi.org/10.1128/jb.170.4.1837-1842.1988
28. Xie Y, He Y, Irwin PL, Jin T, Shi X. 2011. Antibacterial activity and mechanism of action of zinc oxide nanoparticles against *Campylobacter jejuni*. Appl Environ Microbiol 77:2325–2331. https://doi.org/10.1128/AEM.02149-10
29. Joshi SG, Cooper M, Yost A, Paff M, Ercan UK, Fridman G, Friedman G, Fridman A, Brooks AD. 2011. Nonthermal dielectric-barrier discharge plasma-induced inactivation involves oxidative DNA damage and membrane lipid peroxidation in *Escherichia coli*. Antimicrob Agents Chemother 55:1053–1062. https://doi.org/10.1128/AAC.01002-10
30. Citterio B, Casaroli A, Pierfelici L, Battistelli M, Falcieri E, Baffone W. 2004. Morphological changes and outer membrane protein patterns in *Helicobacter pylori* during conversion from bacillary to coccoid form. New Microbiol 27:353–360.
31. Fernández-Castané A, Li H, Thomas ORT, Overton TW. 2017. Flow cytometry as a rapid analytical tool to determine physiological responses to changing O_2 and iron concentration by *Magnetospirillum gryphiswaldense* strain MSR-1. Sci Rep 7:13118. https://doi.org/10.1038/s41598-017-13414-z
32. Wang Y, Lin W, Li J, Pan Y. 2013. Changes of cell growth and magnetosome biomineralization in *Magnetospirillum magneticum* AMB-1 after ultraviolet-B irradiation. Front Microbiol 4:397. https://doi.org/10.3389/fmicb.2013.00397
33. Fernández-Castané A, Li H, Ebeler M, Franzreb M, Overton TW, Thomas ORT. 2024. A scalable biomanufacturing platform for bacterial magnetosomes. Food and Bioproducts Processing 144:110–122. https://doi.org/10.1016/j.fbp.2024.01.005
34. Silva KT, Abreu F, Keim CN, Farina M, Lins U. 2008. Ultrastructure and cytochemistry of lipid granules in the many-celled magnetotactic prokaryote, "*Candidatus Magnetoglobus multicellularis*". Micron 39:1387–1392. https://doi.org/10.1016/j.micron.2008.05.009
35. Obruca S, Sedlacek P, Slaninova E, Fritz I, Daffert C, Meixner K, Sedrlova Z, Koller M. 2020. Novel unexpected functions of PHA granules. Appl Microbiol Biotechnol 104:4795–4810. https://doi.org/10.1007/s00253-020-10568-1
36. Batista MB, Teixeira CS, Sfeir MZT, Alves LPS, Valdameri G, Pedrosa F de O, Sassaki GL, Steffens MBR, de Souza EM, Dixon R, Müller-Santos M. 2018. PHB biosynthesis counteracts redox stress in *Herbaspirillum seropedicae* Front Microbiol 9:472. https://doi.org/10.3389/fmicb.2018.00472
37. Montano-Herrera L, Laycock B, Werker A, Pratt S. 2017. The evolution of polymer composition during PHA accumulation: the significance of reducing equivalents. Bioengineering (Basel) 4:20. https://doi.org/10.3390/bioengineering4010020
38. Su Q, Bazylinski DA, Jensen MM. 2023. Effect of oxic and anoxic conditions on intracellular storage of polyhydroxyalkanoate and polyphosphate in *Magnetospirillum magneticum* strain AMB-1. Front Microbiol 14:1203805. https://doi.org/10.3389/fmicb.2023.1203805
39. Koskimäki JJ, Kajula M, Hokkanen J, Ihantola E-L, Kim JH, Hautajärvi H, Hankala E, Suokas M, Pohjanen J, Podolich O, Kozyrovska N, Turpeinen A, Pääkkönen M, Mattila S, Campbell BC, Pirttilä AM. 2016. Methyl-esterified 3-hydroxybutyrate oligomers protect bacteria from hydroxyl radicals. Nat Chem Biol 12:332–338. https://doi.org/10.1038/nchembio.2043
40. Obruca S, Marova I, Svoboda Z, Mikulikova R. 2010. Use of controlled exogenous stress for improvement of poly(3-hydroxybutyrate) production in *Cupriavidus necator*. Folia Microbiol (Praha) 55:17–22. https://doi.org/10.1007/s12223-010-0003-z
41. Obruca S, Marova I, Stankova M, Mravcova L, Svoboda Z. 2010. Effect of ethanol and hydrogen peroxide on poly(3-hydroxybutyrate) biosynthetic pathway in *Cupriavidus necator* H16. World J Microbiol Biotechnol 26:1261–1267. https://doi.org/10.1007/s11274-009-0296-8
42. Hierro-Iglesias C, Masó-Martínez M, Dulai J, Chong KJ, Blanco-Sanchez PH, Fernández-Castané A. 2021. Magnetotactic bacteria-based biorefinery: potential for generating multiple products from a single fermentation. ACS Sustainable Chem Eng 9:10537–10546. https://doi.org/10.1021/acssuschemeng.1c02435
43. Malik A, Nath M, Mohiyuddin S, Packirisamy G. 2018. Multifunctional CdSNPs@ZIF-8: potential antibacterial agent against GFP-expressing *Escherichia coli* and *Staphylococcus aureus* and efficient photocatalyst for degradation of methylene Blue. ACS Omega 3:8288–8308. https://doi.org/10.1021/acsomega.8b00664
44. Manoil D. 2018. Oxidative stress in bacteria measured by flow cytometry. AIBM 8. https://doi.org/10.19080/AIBM.2018.08.555726
45. Wang Q, Liu JX, Zhang WJ, Zhang TW, Yang J, Li Y. 2013. Expression patterns of key iron and oxygen metabolism genes during magnetosome formation in *Magnetospirillum gryphiswaldense* MSR-1. FEMS Microbiol Lett 347:163–172. https://doi.org/10.1111/1574-6968.12234
46. McBee ME, Chionh YH, Sharaf ML, Ho P, Cai MWL, Dedon PC. 2017. Production of superoxide in bacteria is stress- and cell state-dependent: a gating-optimized flow cytometry method that minimizes ROS measurement artifacts with fluorescent dyes. Front Microbiol 8:459. https://doi.org/10.3389/fmicb.2017.00459
47. Cornelis P, Wei Q, Andrews SC, Vinckx T. 2011. Iron homeostasis and management of oxidative stress response in bacteria. Metallomics 3:540–549. https://doi.org/10.1039/c1mt00022e
48. Faivre D, Menguy N, Posfai M, Schuler D. 2008. Environmental parameters affect the physical properties of fast-growing magnetosomes. American Mineralogist 93:463–469. https://doi.org/10.2138/am.2008.2678
49. Moisescu C, Ardelean II, Benning LG. 2014. The effect and role of environmental conditions on magnetosome synthesis. Front Microbiol 5:1–12. https://doi.org/10.3389/fmicb.2014.00049
50. Meldrum FC, Mann S, Heywood BR, Frankel RB, Bazylinski DA. 1993. Electron microscopy study of magnetosomes in a cultured coccoid magnetotactic bacterium. Proc R Soc Lond B 251:231–236. https://doi.org/10.1098/rspb.1993.0034
51. Nudelman H, Zarivach R. 2014. Structure prediction of magnetosome-associated proteins. Front Microbiol 5:9. https://doi.org/10.3389/fmicb.2014.00009
52. Riese CN, Uebe R, Rosenfeldt S, Schenk AS, Jérôme V, Freitag R, Schüler D. 2020. An automated oxystat fermentation regime for microoxic cultivation of *Magnetospirillum gryphiswaldense*. Microb Cell Fact 19:206. https://doi.org/10.1186/s12934-020-01469-z
53. Pang B, Zheng H, Ma S, Tian J, Wen Y. 2024. Nitric oxide sensor NsrR is the key direct regulator of magnetosome formation and nitrogen metabolism in *Magnetospirillum*. Nucleic Acids Res 52:2924–2941. https://doi.org/10.1093/nar/gkad1230
54. Amor M, Tharaud M, Gélabert A, Komeili A. 2020. Single-cell determination of iron content in magnetotactic bacteria: implications for the iron biogeochemical cycle. Environ Microbiol 22:823–831. https://doi.org/10.1111/1462-2920.14708

55. Amor M, Ceballos A, Wan J, Simon CP, Aron AT, Chang CJ, Hellman F, Komeili A. 2020. Magnetotactic bacteria accumulate a large pool of iron distinct from their magnetite crystals. Appl Environ Microbiol 86:1–20. https://doi.org/10.1128/AEM.01278-20
56. Berny C, Le Fèvre R, Guyot F, Blondeau K, Guizonne C, Rousseau E, Bayan N, Alphandéry E. 2020. A Method for producing highly pure magnetosomes in large quantity for medical applications using *Magnetospirillum gryphiswaldense* MSR-1 magnetotactic bacteria amplified in minimal growth media. Front Bioeng Biotechnol 8. https://doi.org/10.3389/fbioe.2020.00016
57. Faivre D, Böttger LH, Matzanke BF, Schüler D. 2007. Intracellular magnetite biomineralization in bacteria proceeds by a distinct pathway involving membrane - bound ferritin and an iron(II) species. Angew Chem Int Ed 46:8495–8499. https://doi.org/10.1002/anie.200700927
58. Amor M, Busigny V, Louvat P, Tharaud M, Gélabert A, Cartigny P, Carlut J, Isambert A, Durand-Dubief M, Ona-Nguema G, Alphandéry E, Chebbi I, Guyot F. 2018. Iron uptake and magnetite biomineralization in the magnetotactic bacterium *Magnetospirillum magneticum* strain AMB-1: An iron isotope study. Geochim Cosmochim Acta 232:225–243. https://doi.org/10.1016/j.gca.2018.04.020
59. Uebe R, Ahrens F, Stang J, Jäger K, Böttger LH, Schmidt C, Matzanke BF, Schüler D. 2019. Bacterioferritin of *Magnetospirillum gryphiswaldense* is a heterotetraeicosameric complex composed of functionally distinct subunits but is not involved in magnetite biomineralization. mBio 10:1–13. https://doi.org/10.1128/mBio.02795-18
60. Fernández-Castané A, Clarke-Bland C. 2019. Unveiling magnetosome biomineralization in magnetotactic bacteria. Biochem (Lond) 41:58–59. https://doi.org/10.1042/BIO04104058
61. Chevrier DM, Cerdá-Doñate E, Park Y, Cacho-Nerin F, Gomez-Gonzalez M, Uebe R, Faivre D. 2022. Synchrotron-based nano-x-ray absorption near-edge structure revealing intracellular heterogeneity of iron species in magnetotactic bacteria. Small Sci 2:2100089. https://doi.org/10.1002/smsc.202100089
62. Qi L, Li J, Zhang WJ, Liu J, Rong C, Li Y, Wu L. 2012. Fur in *Magnetospirillum gryphiswaldense* influences magnetosomes formation and directly regulates the genes involved in iron and oxygen metabolism. PLoS One 7:e29572. https://doi.org/10.1371/journal.pone.0029572
63. Wang Q, Wang M, Wang X, Guan G, Li Y, Peng Y, Li J. 2015. Iron response regulator protein IrrB in *Magnetospirillum gryphiswaldense* MSR-1 helps control the iron/oxygen balance, oxidative stress tolerance, and magnetosome formation. Appl Environ Microbiol 81:8044–8053. https://doi.org/10.1128/AEM.02585-15
64. Rong C, Zhang C, Zhang Y, Qi L, Yang J, Guan G, Li Y, Li J. 2012. FeoB2 Functions in magnetosome formation and oxidative stress protection in *Magnetospirillum gryphiswaldense* strain MSR-1. J Bacteriol 194:3972–3976. https://doi.org/10.1128/JB.00382-12
65. Altuvia S, Almirón M, Huisman G, Kolter R, Storz G. 1994. The dps promoter is activated by OxyR during growth and by IHF and sigma S in stationary phase. Mol Microbiol 13:265–272. https://doi.org/10.1111/j.1365-2958.1994.tb00421.x
66. Escolar L, Pérez-Martín J, de Lorenzo V. 1998. Binding of the fur (ferric uptake regulator) repressor of *Escherichia coli* to arrays of the GATAAT sequence. J Mol Biol 283:537–547. https://doi.org/10.1006/jmbi.1998.2119
67. Petrat F, Rauen U, de Groot H. 1999. Determination of the chelatable iron pool of isolated rat hepatocytes by digital fluorescence microscopy using the fluorescent probe, phen green SK. Hepatology 29:1171–1179. https://doi.org/10.1002/hep.510290435